Chapter 2
Nanoparticles

List of Abbreviations

Polymers and Other Organic Compounds

DMF	*N*,*N*-dimethylformamide
PMMA	Poly(methyl methacrylate)
TEOS	Tetraethyl orthosilicate
TMOS	Tetramethyl orthosilicate
TPO	Thermoplastic olefin

Reinforcements

CNFs	Carbon nanofibers
CNTs	Carbon nanotubes
GIC	Graphite intercalation compound
GO	Graphite oxide
LDH	Layered double hydroxide
MMT	Montmorillonite
MWCNT	Multi-walled carbon nanotube
POSS	Polyhedral oligomeric silsesquioxane
SWCNT	Single-walled carbon nanotube

Characterization Techniques

AFM	Atomic force microscopy
SEM	Scanning electron microscopy
XRD	X-ray diffraction

Others

CEC	Cation exchange capacity
CVD	Chemical vapor deposition

A. Dasari et al., *Polymer Nanocomposites*, Engineering Materials and Processes, DOI 10.1007/978-1-4471-6809-6_2

2.1 Introduction

By definition, nanoparticles have at least one characteristic dimension of less than 100 nm. They exhibit properties that are different to their respective micro- and macroscale counterparts with the same chemical compositions. Auffan et al. [1] concluded that there is a critical size, which is considerably smaller than 100 nm, at which properties of particles change. They identified this critical size of ~20–30 nm by relating the exponential increase in the number of atoms localized at the surface to the size of the nanoparticles (Fig. 2.1a). A simple visual representation of this phenomenon is shown in Fig. 2.1b [2]. The fraction of atoms or molecules located at the surface dramatically increases as the side length is reduced to 10 nm. Specifically, this phenomenon is shown as a function of particle size for different shaped particles in Fig. 2.2 [3, 4].

To probe the distribution of atoms at the surfaces of iron oxide particles (in turn size-dependent properties), Yean et al. [5] used arsenic as an adsorbent. They found that the quantity of arsenic adsorbed per gram of iron oxide increased from 0.02 to 1.8 mmol g^{-1} as particle size decreased from 300 to 11 nm. However, when normalized by specific surface area, both 300 and 20 nm iron oxide particles seem to adsorb similar amounts of arsenic (~6 mmol m^{-2} or 3.6 atoms nm^{-2}). Therefore, the increase in the number of surface reactive sites cannot explain the threefold increase in adsorption capacity with 11 nm particles (~18 mmol m^{-2} or 11 atoms nm^{-2}). It is also estimated that the maximum number of molecules that can adsorb onto the surface is ~4 atoms nm^{-2} [6]. Based on other set of results on maghemite (γ-Fe_2O_3) [7], it is suggested that the enhanced adsorption capacity is due to the changes in surface structure resulting in new surface adsorption sites and a significant decrease of the surface energy (Fig. 2.3) [1].

Moreover, the excessive increase in surface energy of nanoparticles results in crystallographic changes and subsequently affects their interfacial reactivity (Fig. 2.4) and intrinsic properties [1, 8, 9]. Catalytic activity, for instance, is related to particle size and type of exposed crystalline faces [7, 10]. Boehmite exhibits size-dependent change in morphology and interfacial reactivity between 10 and 100 nm [11]. By controlling the pH and the ionic strength in the medium of synthesis, different sized particles are obtained. 100-nm-sized γ-AlOOH are fibers or rods, and they are formed by aggregation of very small platelets (3 nm thick and 6 nm wide) with (100) lateral faces and (010) basal planes. However, 10–25-nm-sized particles are diamond-shaped with (101) lateral faces. Therefore, size changes are strongly reflected in a change of the (area) ratio between (100), (010), and (101) faces of crystallographic planes (Fig. 2.5). This influences the surface charge density and surface energy of these particles, subsequently affecting their reactivity in a polymer [9]. A well-known example is comparison between Ag nanoparticles (which exhibit biocidal effect) and bulk Ag (which displays no biocidal activity) [12]. Even in bulk ferromagnetic materials where multiple magnetic domains exist, several small ferromagnetic particles consisting of only a single magnetic domain result in superparamagnetism [13].

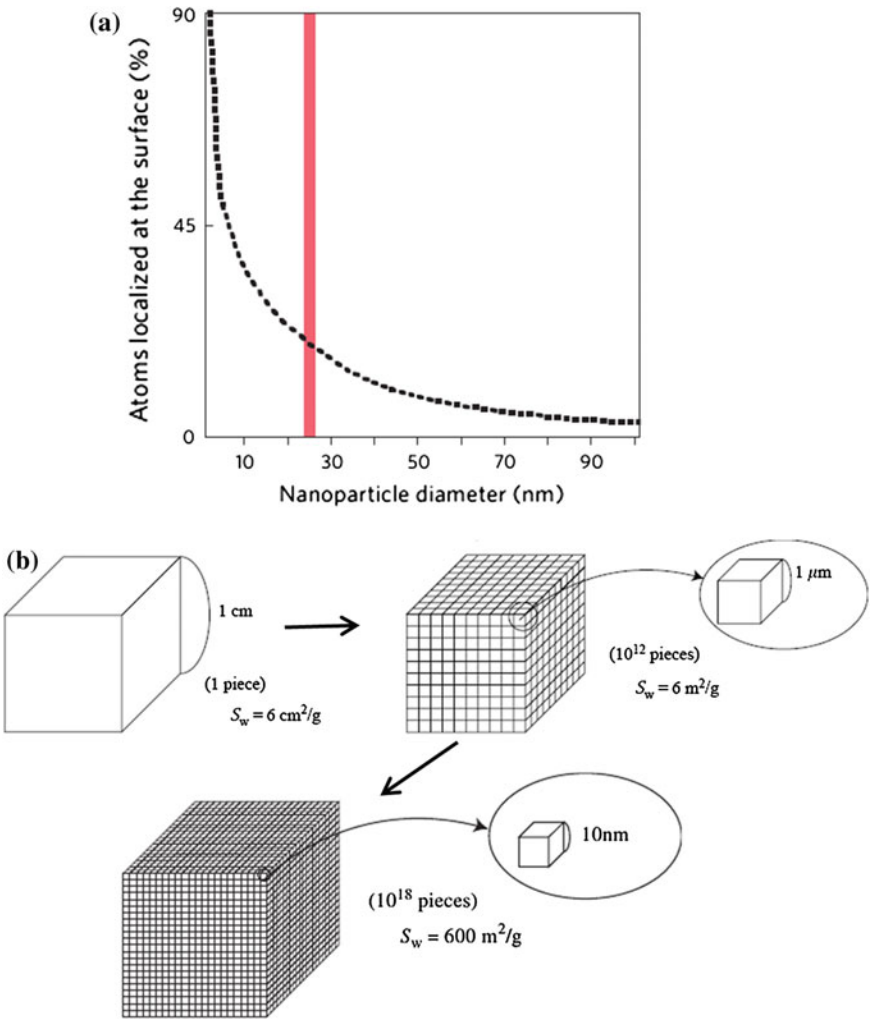

Fig. 2.1 **a** Plot showing the correlation between atoms localized at the surface of a nanoparticle and its diameter; *red line* indicates the transition between bulk and non-bulk properties. **b** Changes in specific surface area (S_w) of a cube (solid, density 1 g/cm^3) by changing the side length. (**a**) is reprinted by permission from Macmillan Publishers Ltd: Nature Nanotechnology [1], Copyright (2009); and (**b**) is reprinted from [2], Copyright (2008), with permission from Elsevier (Color figure online)

Another well-known example of 'size effect' is the change in melting point [14]. As the localized number of atoms at the particle surface increases and becomes influential, the melting point of the material decreases from that of the bulk material. For instance, the melting point of gold (in bulk state) is 1336 K, but it decreases

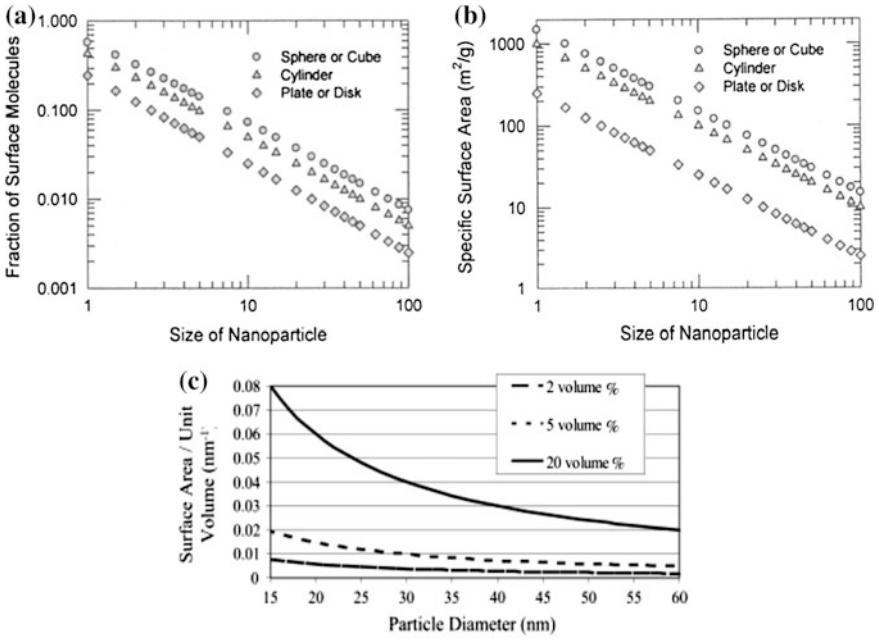

Fig. 2.2 Calculated **a** fraction of surface molecules and **b** specific surface area as a function of particle size for different dimension particles (size refers to diameter in the case of spherical and cylinder particles, the side for a cube and the thickness for a plate or a disk); and **c** surface area per unit volume as a function of particle size for spherical particles that are homogeneously dispersed. (**a**, **b**) are reprinted with permission from [3], Copyright (2008) American Chemical Society; and (**c**) is reprinted with permission from [4], Copyright (2004) John Wiley and Sons

below the particle size of about 20 nm. Hence, at ~2 nm, the melting point is lowered by more than 500 K than that of bulk gold [15]. Similarly, the melting point of indium and tin nanoparticles is reduced by 120 °C [16] and 80 °C [17], respectively, by decreasing their diameters from 100 to 10 nm. In some nanoparticles such as $BaTiO_3$, a change in particle size has also been correlated to changes in crystal structure based on c/a ratio (Fig. 2.6) [10]. This is attributed to the compressive force exerted on the particles as a result of the surface tension of the particle itself. Even size dependence of optical and electronic properties has been well reported [18]. For instance, electroluminescence of semiconducting nanoparticles is size-dependent [4]. Similar concept applies for electrical breakdown strength.

The above discussion means that their (nanoparticles) presence in a system (polymer, metal, or ceramic) provides an opportunity to alter many of the base properties of the system. Moreover, nanoparticles do not create large stress concentrations when incorporated in a matrix due to their small size and thus do not compromise mechanical properties. It is predicted that the replacement of 25–35 %

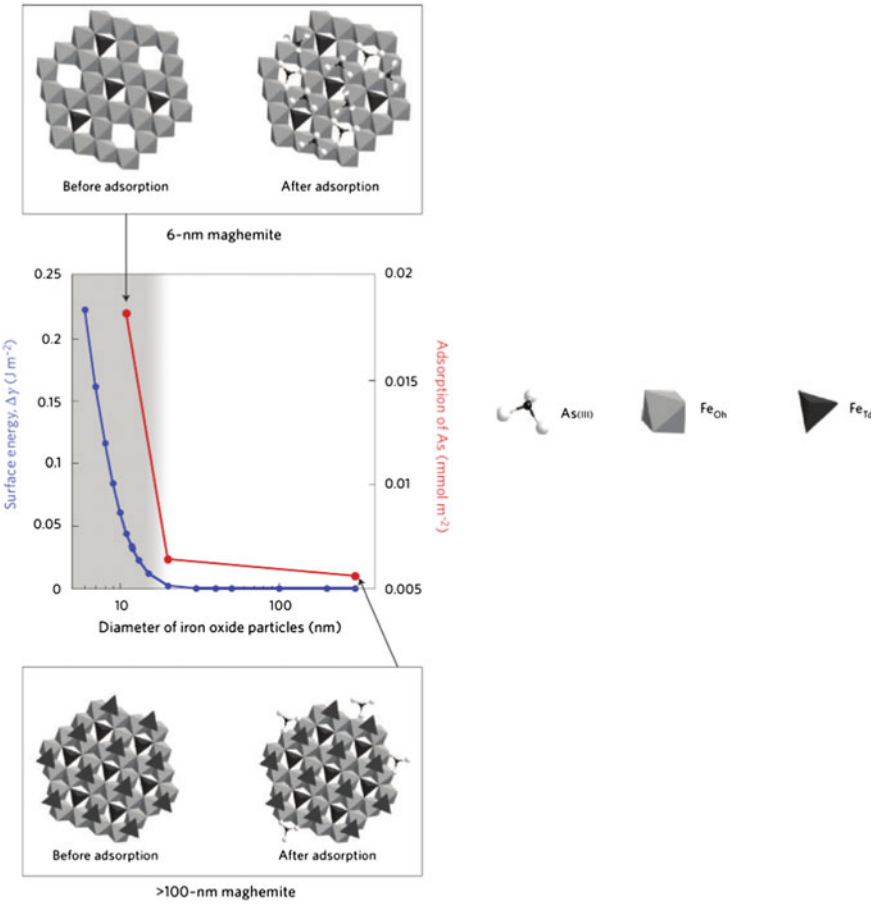

Fig. 2.3 Size dependence of the mechanisms of arsenic adsorption on the surface of iron oxide particles. Evidently, both surface energy and adsorption capacity change significantly for particle diameters below about 20 nm. As the size decreases, the occupancy of the tetrahedral site decrease, creating unique and highly reactive adsorption sites in the crystal lattice position. Reprinted by permission from Macmillan Publishers Ltd: Nature Nanotechnology [1], Copyright (2009)

talc-filled TPO composites (conventionally used in automotive industry) by 5 % clay (smectite)-filled TPO nanocomposites could save up to 1.5 billion liters of gasoline over the life of one year's production of vehicles with an added advantage of reduced CO_2 emissions by more than 5 billion kilograms and improved mechanical performance [19].

The dramatic improvement in interfacial area clearly suggests that 'interface' controls the degree of interaction between filler and matrix and thus the ultimate properties. Hence, the greatest challenge in developing nanocomposites is the ability to control the interactions between matrix and nanoparticles through physical interaction or chemical bonding. Equally challenging is the homogeneous

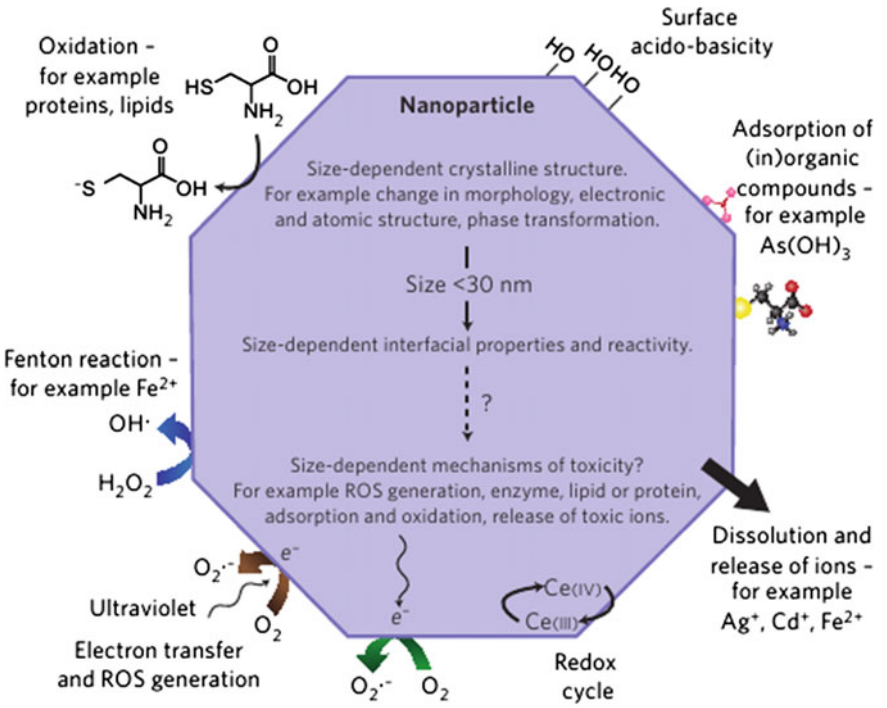

Fig. 2.4 Physicochemical mechanisms occurring at the surface of an inorganic nanoparticle [1]. Relationship between size, interfacial properties (dissolution, oxidation, adsorption/desorption, electron transfer, redox cycles, reactive oxygen species (ROS) generation, etc.) and potential mechanisms of toxicity. Reprinted by permission from Macmillan Publishers Ltd: Nature Nanotechnology [1], Copyright (2009)

dispersion of the nanoparticles in a matrix. As nanoparticles can occur naturally (like clay minerals) or generated via a number of synthetic routes (based on gas-, liquid-, or solid-phase approaches), the refined/synthesized nanoparticles must be surface modified in most cases. More specific details on the surface modification techniques of nanoparticles and processing of nanocomposites will be discussed in Chap. 3.

As cohesion of nanoparticles increases with increasing particle surface energy, researchers have studied the application of composite structures for proper handling of these particles. This, in turn, induced new functionality (with some nanoparticles) to these structures. Some examples of these structures are shown in Fig. 2.7 [2]. Nevertheless, in this chapter, only an overview of different inorganic nanoparticles along with their advantages and disadvantages is presented. The emphasis will be placed only on those widely used for incorporation in polymers.

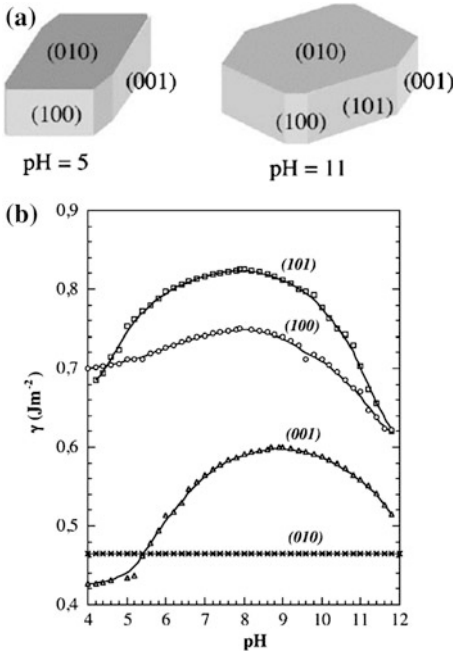

Fig. 2.5 **a** Different morphologies of boehmite particles calculated based on XRD data. As is well-known, variations of interfacial tension of different faces **b** induce preferential growth of the (100) or (101) faces depending on the pH. Since the interfacial tension of the (010) faces is the lowest and independent of pH, growth dominates along these faces. Reproduced from [9] with permission of The Royal Society of Chemistry, Copyright (2008)

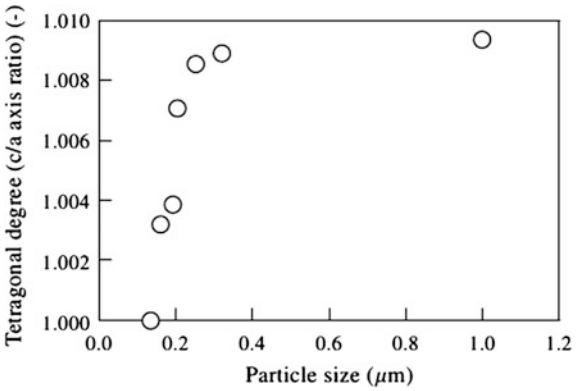

Fig. 2.6 Relation between $BaTiO_3$ particle size and tetragonal degree (c/a axis ratio). Reprinted from [2], Copyright (2008), with permission from Elsevier

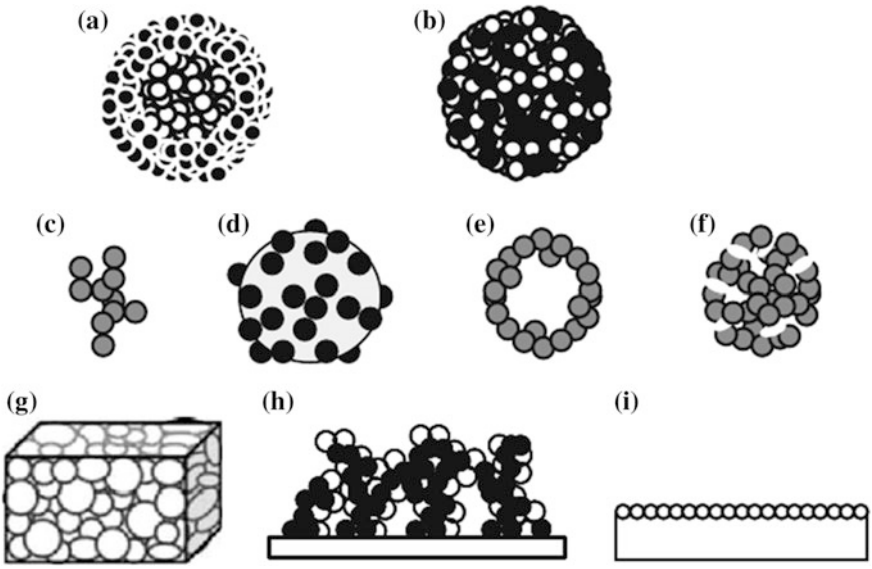

Fig. 2.7 Composite structures produced from nanoparticles. **a** Core shell. **b** Internal dispersion. **c** Agglomeration. **d** Nanoparticle coating. **e** Hollow. **f** Porous. **g** Bulk body form nanograins. **h** Porous body from nanograins. **i** Nano thin film. Reprinted from [2], Copyright (2008), with permission from Elsevier

2.2 Different Types of Nanoparticles

2.2.1 Clay Minerals

Clay minerals have thickness, typically, a few nanometers, and the other two dimensions in the submicron range. Most of the clay minerals exist naturally as stacks and hundreds or thousands of these layers are stacked together by van der Waals forces (and in some cases, electrostatic forces) [20–23]. As a result, these fillers are difficult to disperse individually in polymers owing to their large contact areas between particles and enhanced particle–particle interaction. Still, this configuration provides an excellent opportunity for fine-tuning their surface chemistry through ion exchange reactions with organic and inorganic cations. This leads to many possibilities and prospects for tailoring various required properties for specific end applications, more than just merely dispersing the layers in a polymer matrix. Apart from the *layered* silicates, which include natural and/or artificial magadiite, bentonite, kaolinite, montmorillonite, saponite, vermiculite, talc, hectorite, attapulgite, fluoromica, and chlorite, many others with different geometry have also been used to make nanocomposites. Some of them include sepiolite (*needle/fiber-like*), halloysite (*tube-like*), kaolinite (*vermicular*), and layered double hydroxides (*platelet-shaped*).

Table 2.1 Classification of clay minerals (phyllosilicates)

Type	Group	Species	Tetrahedron	Octahedron	Interlayer cation
2:1 $Si_4O_{10}(OH)_2$	Pyrophyllite, Talc ($x \sim 0$)	Pyrophyllite (di)	Si_4	Al_2	–
		Talc (tri)	Si_4	Mg_3	–
	Smectite ($0.25 < x < 0.6$)	Montmorillonite (di)	Si_4	$(Al_2, Mg)_2$	Na, Ca, H_2O
		Hectorite (di)	Si_4	$(Mg_2, Li)_2$	Na, Ca, H_2O
		Beidellite (di)	$(Si, Al)_4$	Al_2	Na, Ca, H_2O
		Saponite (tri)	$(Si, Al)_4$	Mg_3	Na, Ca, H_2O
	Vermiculite ($0.25 < x < 0.9$)	Vermiculite (di)	$(Si, Al)_4$	$(Al, Mg)_2$	K, Al, H_2O
		Vermiculite (tri)	$(Si, Al)_4$	$(Mg, Al)_3$	K, Mg, H_2O
	Mica ($x \sim 1$)	Muscovite (di)	$Si_3{\cdot}Al$	Al_2	K
		Paragonite (di)	$Si_3{\cdot}Al$	Al_2	Na
	Brittle mica ($x \sim 2$)	Phlogopite (tri)	$Si_3{\cdot}Al$	$(Mg, Fe^{2+})_3$	K
		Biotite (tri)	$Si_3{\cdot}Al$	$(Fe^{2+}, Mg)_3$	K
2:1:1 $Si_4O_{10}(OH)_8$	Chlorite (large variation of x)	Donbassite (di)	$(Si, Al)_4$	Al_2	$Al_2(OH)_6$
		Clinochlore (tri)	$(Si, Al)_4$	$(Mg, Al)_3$	$(Mg, Al)_3(OH)_6$
		Chamosite (tri)	$(Si, Al)_4$	$(Fe, Al)_3$	$(Fe, Al)_3(OH)_6$
1:1 $Si_2O_5(OH)_4$	Kaolin, Serpentinite ($x \sim 0$)	Kaolinite (di)	Si_2	Al_2	–
		Halloysite (di)	Si_2	Al_2	H_2O
Needle	Sepiolite, Palygorskite ($x \sim 0$)	Sepiolite (tri)	Si_{12}	Mg_8	$(OH_2)_4{\cdot}H_2O$
		Palygorskite (tri)	Si_8	Mg_8	$(OH_2)_4{\cdot}H_2O$

Adapted from [24]
x—Degree of isomorphous substitution; di—dicotahedral; and tri—trioctahedral

Clay minerals are commonly classified based on their crystalline structure. Different types of clay minerals with representative examples are listed in Table 2.1 [24], and electron microscopy images of some selected clay minerals with different particle morphologies are shown in Fig. 2.8 [25–28]. Among these, the most commonly used morphologies for the preparation of polymer nanocomposites belong to the family of 2:1 phyllosilicates and, in particular, smectite clays because of their swelling properties and high values of CEC. In the family of 2:1 type, crystal structure is made up of layers of two tetrahedrally coordinated silicon atoms fused to an edge-shared octahedral sheet of either aluminum or magnesium hydroxide (Fig. 2.9a) [29–31]. The layer thickness is $\sim$0.94 nm and has a stiffness of $\sim$170 GPa, and the lateral dimensions vary from 30 nm to several microns, depending on the particular layered silicate (e.g., saponite $\sim$50–60 nm; montmorillonite $\sim$100–150 nm; hectorite $\sim$200–300 nm). This provides a large surface area $\sim$700–900 m^2/g of silicate material.

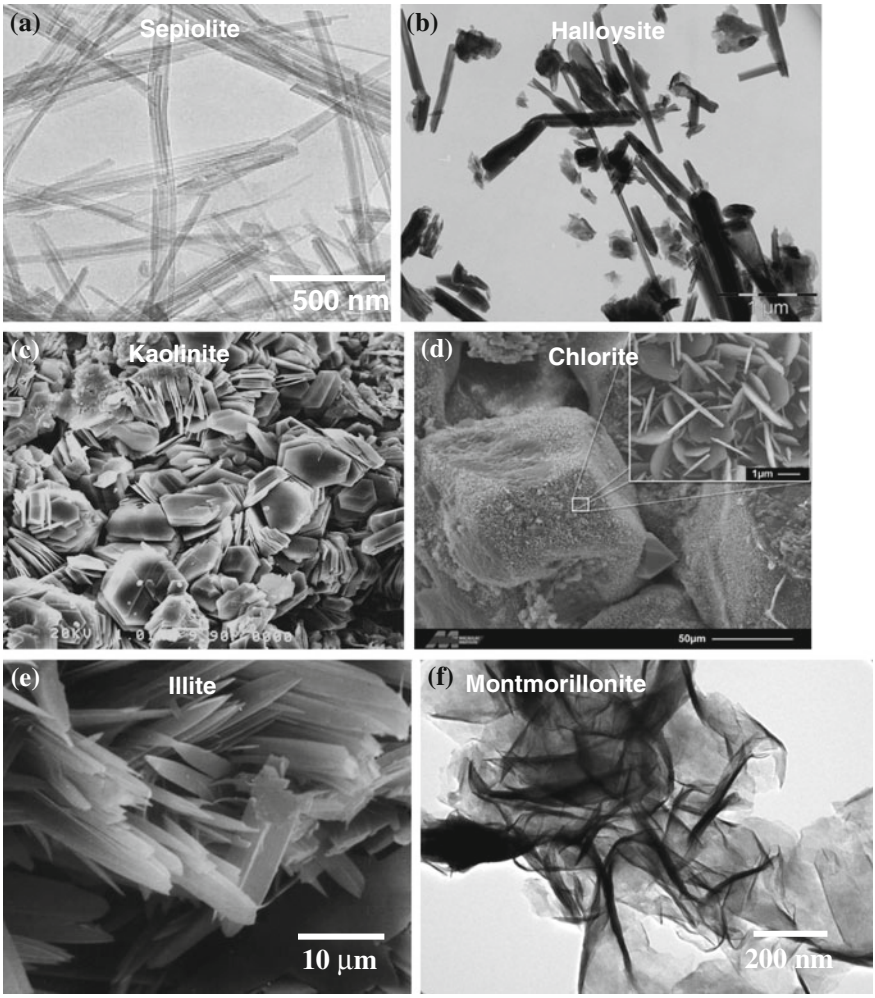

Fig. 2.8 Some commonly used clay minerals with different particle shapes: **a** fibrous sepiolite, **b** tube-like halloysite, **c** vermicular kaolinite, **d** chlorite, **e** lath-shaped illite, and **f** layered montmorillonite. (**a**) is reproduced from [26] with permission of John Wiley and Sons, Copyright (2008); (**d**) is reprinted from [25] with permission of Springer Netherlands, Copyright (2003)

As mentioned before, these layers organize themselves into stacks leading to a regular van der Waals gap between the layers known as the interlayer or intra-gallery. Isomorphic substitution within the layers (e.g., Al^{3+} replaced by Mg^{2+} or by Fe^{2+}, or Mg^{2+} replaced by Li^{+}) generates negative charges (each unit cell has a negative charge between 0.5 and 1.3) which are generally counterbalanced by alkali or alkaline earth cations located in the interlayer. Thus, this type of clay is characterized by a moderate negative surface charge, CEC, that is an important factor during the fabrication of nanocomposites as it determines the amount of

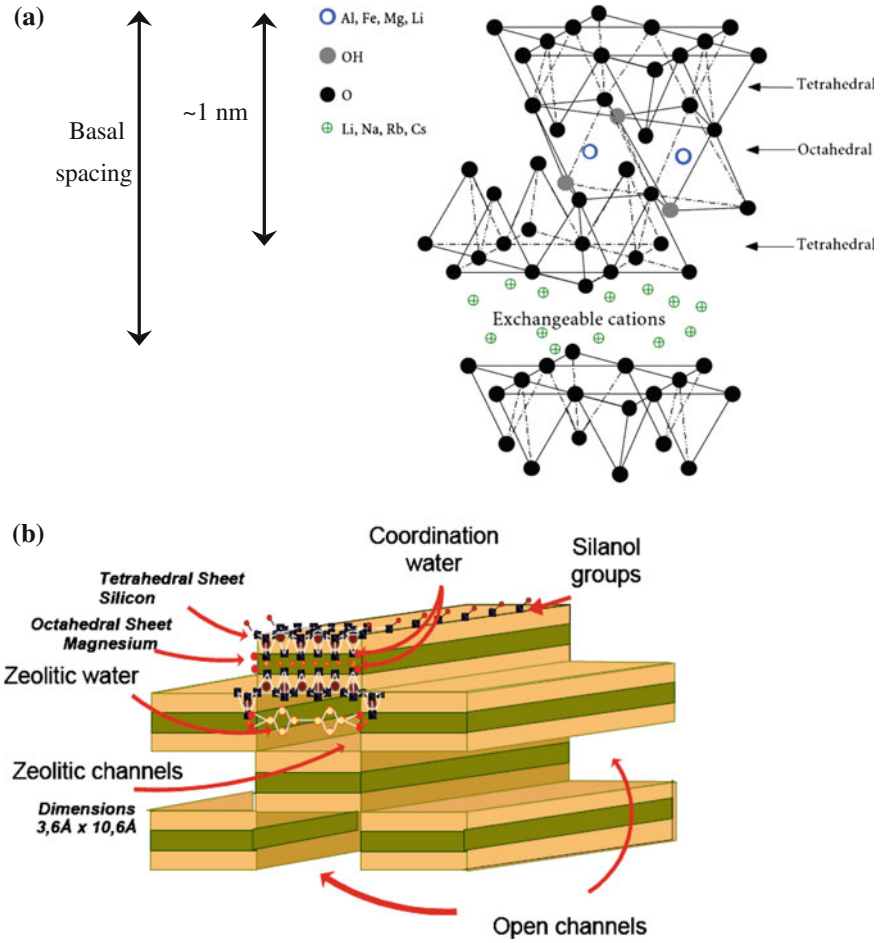

Fig. 2.9 Schematic of crystal structure of **a** 2:1 phyllosilicates (bentonite) and **b** sepiolite. (**a**) is reproduced from [29] with kind permission from Springer Science, Copyright (1999); and for reproducing (**b**), Tolsa S.A. is acknowledged

surfactants that can be intercalated between silicate layers (into the intra-gallery). This renders the hydrophilic phyllosilicates more organophilic and compatible with organic polymers (for more details, see Chap. 3). For example, consider Na-MMT, for which the unit cell can be expressed as [32]:

Triple layer sandwich of two silica tetrahedron sheets and a central octahedral sheet with 0.67 negative charge per unit cell	$\left[Al_{3.33}Mg_{0.67}\right]^{-(0.67)}Si_8O_{20}(OH)_4$
	$\Downarrow$
Aqueous interlamellar layer containing 0.67 Na^+ cations per unit cell	$(n \times H_2O)Na^+_{0.67}$

Therefore, an 'ideal' MMT has 0.67 units of negative charge per unit cell. Since the molecular weight of a unit cell is 734+ water, the CEC will be 0.915 meq/g (one ion per 1.36 nm^2).

Nevertheless, the basic requirement is that the polarities of organoclay and the monomer or prepolymer should match. That is, their role is to lower the surface energy of the inorganic host and improve the wetting characteristics with the polymer matrix. Considering the density of Na^+ as 0.67 Na^+/nm^2, almost 6700 alkylammonium salt molecules (commonly used surfactant) are localized near the individual silicate layer! Further, assuming that hydroxyl groups are randomly distributed on the silicate edge surface, this results in a Si-OH density of 5Si-OH/nm^2, which means 500 –OH groups are also localized [33]. Balancing these lipophilic (or organophilic) and hydrophobic conditions is a major factor to attain uniform dispersion/distribution of silicate layers in a polymer matrix. Moreover, the source or type of clay mineral (influences the charge density and inherent size of clay platelets) is also crucial in determining the dispersion extent of clay in polymers [34–37]. Thus, it was shown that sodium MMT obtained from Yamagata, Japan, differs in size to that obtained from Wyoming, USA [34]. Yamagata clay comprised of platelets that were slightly larger than those of the Wyoming clay; this difference affected the exfoliation extents when used in PA6 under the same processing and organic modification conditions. This ultimately reflected on the tensile properties between the two PA6/clay nanocomposites.

In contrast to cationic clays described above, LDHs or hydrotalcites or anionic clays are a fairly new class of materials and represented by the formula $\left[M^{II}_{1-x}M^{III}_{x}(OH)_2\right](A^{m-})_{x/m}\cdot mH_2O$ [38–41]. M^{II} represents divalent (or monovalent) cations such as Mg^{2+} and Zn^{2+}, M^{III} trivalent cations such as Al^{3+} and Cr^{3+}, and A interlayer anion with valency m (such as Cl^-, CO_3^{2-}, SO_4^{2-}, and NO_3^-). In general, LDHs have an octahedral structure similar to brucite—$Mg(OH)_2$ where the partial isomorphous replacement of a bivalent cation with a trivalent cation produces positive charges counterbalanced by hydrated anions. Similar to the cationic clays, LDHs can be modified by intercalating organic ions between the lamellas to fabricate nanocomposites. Their lamellar structure and anion exchange properties make them attractive for many applications such as ion-exchangers, adsorbents, pharmaceutical stabilizers, thermal stabilizers, and flame retardants. However, the strong electrostatic attraction between the hydroxide sheets and short interlayer distance makes LDH materials relatively difficult to exfoliate in a polymer [40] when compared to smectite clays.

Apart from these layered fillers, sepiolite (needle-like with open nanotunnels), despite being 'multi-functional' is less represented in the polymer nanocomposites field. They have an average length of 1–2 μm, width ~10 nm, and the dimensions of open channels (along the axis of a particle) ~3.6 Å × 10.6 Å (Fig. 2.9b). The arrangement of these particles results in loosely packed and porous aggregates with an extensive capillary network. It is non-swelling and its granules do not disintegrate even when saturated with liquids. It has the highest surface area of all the clay minerals, about 300 m^2/g, with a high density of the silanol groups (-SiOH), which

manifests its hydrophilicity. Moreover, the high surface area and porosity of sepiolite account for the remarkable adsorptive and absorptive properties.

Other group of layered nanofillers is (layered) silicic acids. Their intercalation chemistry is similar to smectite clays [42, 43]. Examples of layered silicic acids are kanemite ($NaHSi_2O_5$), makatite ($Na_2Si_4)_9{\cdot}nH_2O$), octosilicate ($Na_2Si_8O_{17}{\cdot}nH_2O$), magadiite ($Na_2Si_{13}O_{29}{\cdot}nH_2O$), and kenyaite ($Na_2Si_{20}O_{41}{\cdot}nH_2O$). The thickness of the layers varies from 0.5 nm for makatite to 1.77 nm for kenyaite. The general structure of layered silicic acids consists of layers of SiO_4 tetrahedra with an abundant hydroxyl siloxane surface. Interlayer alkali ions can be exchanged with the resulting active hydroxyl sites, leading to enhanced bonding with the intercalates. Transition metal-based compounds such as titanium and tantalum dichalcogenides are also layered materials, but rarely used to make nanocomposites.

2.2.2 Graphite Nanoplatelets

Graphite consists of carbon layers (with covalent and metallic bonding within each layer) that are stacked in an AB sequence (i.e., different from the AB sequence in a hexagonal close packed or HCP crystal structure) and are linked by a weak van der Waals interaction produced by a delocalized π-orbital [44–48]. The carbon layers (also called as graphene sheets) are 1 atom thick, and the carbon bonding involves sp^2 hybridization (trigonal) (Fig. 2.10) [47]. As graphite is anisotropic, it exhibits good electrical and thermal conductivities within the layers (due to the in-plane metallic bonding) and relatively poor conductivities normal to the layers (due to the weak van der Waals forces between the layers). The anisotropic nature also allows graphite to undergo chemical reactions by allowing the reactant to reside between the graphene layers, resulting in GICs [46].

It has been reported that the mechanical strength of graphene sheets is comparable to that of carbon nanotubes (described below and which are essentially 'rolled' graphene sheets) [48]. Moreover, the compression of exfoliated graphite results in a material of high lubricity and flexibility. As a result, attempts to harness the above remarkable properties of graphitic sheets to polymers have attracted increasing attention over the past few years. But there are certain problems to obtain individual graphene sheets (thickness of one layer is equal to the interlayer separation in graphite, 0.34 nm) and particularly to disperse them at a nanoscale in a

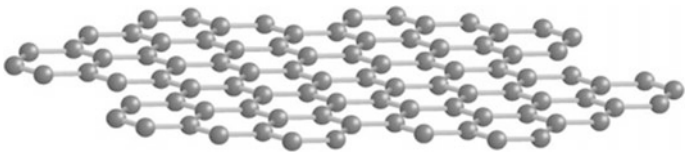

Fig. 2.10 Schematic representation of a graphene sheet. Carbon atoms are bonded together through sp^2 hybridization. Reprinted from [47], Copyright (2007), with permission from Elsevier

Table 2.2 List of different methods for the oxidation of graphite to graphite oxide

	Method (year)			
	Staudenmaier (1898)	Hummers (1958)	Modified Hummers	
			1999	2004
Oxidants	$KClO_3$ (or $NaClO_3$), HNO_3, H_2SO_4	$NaNO_3$, $KMnO_4$, H_2SO_4	Pre-ox: $K_2S_2O_8$, P_2O_5, H_2SO_4	$NaNO_3$, $KMnO_4$, H_2SO_4
C:O ratio	N/A	2.25	1.3	1.8
Reaction time	1–2 days	2 h	6 h pre-ox + 2 h ox	5 days

Adapted from [60]

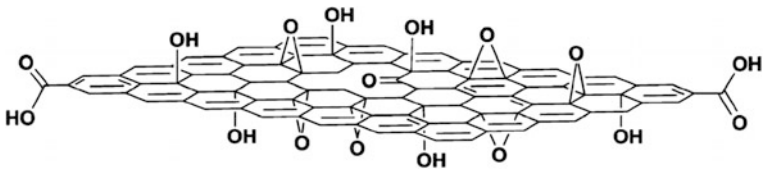

Fig. 2.11 Schematic of a graphene oxide sheet showing the functional groups on the surface and at the edges as a result of oxidation. Reproduced from [60], with permission of John Wiley and Sons, Copyright (2010)

polymer matrix to obtain beneficial properties. Several approaches have been adopted to produce graphene sheets including mechanical cleavage of graphite [49, 50], epitaxial growth [51], bottom-up organic synthesis [52], and chemical exfoliation of graphite [44, 53]. The most commonly used methodology is to prepare GO by oxidizing the graphite flakes.

Many different methods for the preparation of GO were reported [54–58] and include the widely used Hummers [56] procedure (see Table 2.2). It has been reported that the extent of graphite oxidation is quantified by the C:O atomic ratio and is dependent upon the technique and reaction time [59, 60]. GO is hydrophilic due to the presence of hydroxyl and epoxide functional groups on their basal planes, in addition to carbonyl and carboxyl groups located at the sheet edges [60] (Fig. 2.11). GO shows an increase in the distance between adjacent sheets, from 3.35 Å in graphite powder to ~6.8 Å. The hydrophilic nature of GO will also allow it to swell and disperse in aqueous media such as water increasing the interlayer distance. Figure 2.12 shows the differences between natural graphite and GO [61].

The above discussion suggests that GO is incompatible with most organic polymers and is electrically insulating (covalent C–O bonds adversely affects electrical conductivity as oxidation breaks up the sp^2—hybridized structure of stacked graphene sheets). Deoxygenation via chemical reduction is necessary to restore electrical conductivity, owing to the restoration of a graphitic network of sp^2 bonds. However, reduction of exfoliated GO in water again results in their irreversible coagulation, which affects the dispersion within a polymer matrix and ultimate properties.

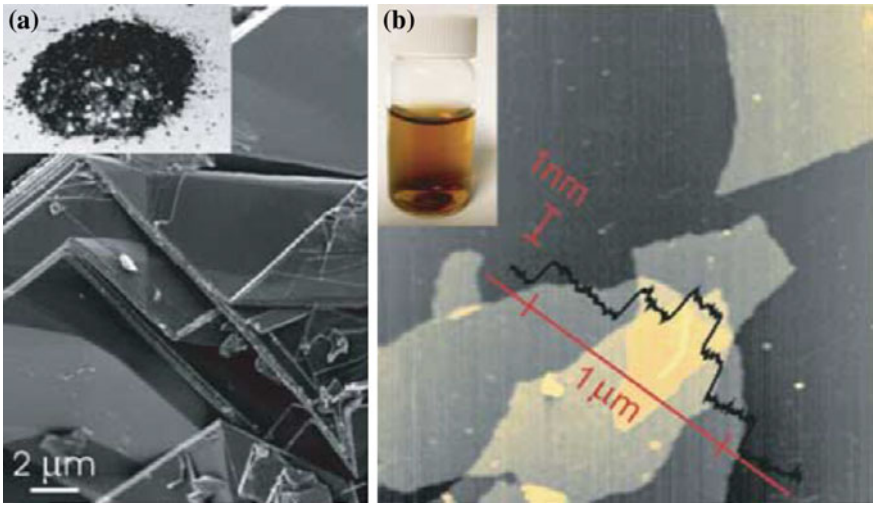

Fig. 2.12 **a** Digital and SEM images of natural graphite; and **b** AFM image of GO sheets deposited onto a mica substrate from an aqueous dispersion (inset) with superimposed cross-sectional measurements taken along the *red line*. Reprinted by permission from Macmillan Publishers Ltd: Nature [61], Copyright (2006) (Color figure online)

Chemical functionalization/treatment of GO is also considered to improve compatibility with polymer matrices. For example, isocyanate treatment reduces the hydrophilic character of GO by forming amide and carbamate ester bonds to the carboxyl and hydroxyl groups of graphite oxide, respectively (Fig. 2.13) [62]. Subsequently, they can form stable dispersions in polar aprotic solvents such as DMF. Coupled with chemical reduction, these dispersions of isocyanate-derivatized GO allows for good compatibility and dispersion with many organic polymers.

Another approach that has been used to prepare individual graphene sheets is by thermal expansion of GO ($\sim$1000 °C under inert conditions) [63–65]. During this process, exfoliation of the stacked structure occurs through release of carbon dioxide, carbon monoxide, water, and other small molecule hydrocarbons by the creation of enormous pressure within the stacked layers. It is noted that the pressure reaches $\sim$40 MPa at 300 °C and increases further to $\sim$130 MPa at 1000 °C. This is also correlated with phenomenal increase in surface area (based on BET tests, it reaches as high as 900 $m^2\ g^{-1}$). However, thermal exfoliation results in vacancies and topological defects throughout the planes of reduced GO sheets affecting electronic properties. Sheets are also crumpled and wrinkled during the thermal process [48].

Solvothermal reduction is another method that is used for removing oxygen-containing groups. Examples include refluxing GO in *N*-methyl-2-pyrrolidinone [66] and refluxing GO in DMF at 140 °C [67]. These processes result in both deoxygenation and reduction to yield a stable colloidal dispersion. Irrespective of these factors, their dispersion in polymer matrix is again a challenging step. We will be discussing more on this in Chap. 3.

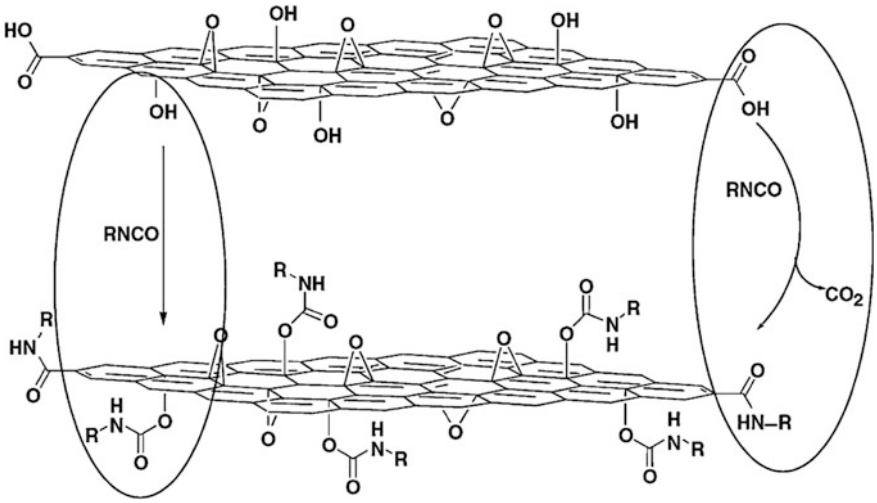

Fig. 2.13 Modification of GO with organic isocyanate in DMF. Isocyanates react with the hydroxyl (*left oval*) and carboxyl groups (*right oval*) of GO sheets to form carbamate and amide functionalities, respectively. Reprinted from [62], Copyright (2006), with permission from Elsevier

2.2.3 Carbon Nanotubes

CNTs are first observed in 1991 by Sumio Iijima [68] while investigating the surface of carbon electrodes used in an electric arc discharge apparatus to make fullerenes. They exhibit properties that are quite different from those of closed-cage fullerenes such as C60, C70, and C76. CNTs can exist as single-walled or multi-walled. They (particularly SWCNTs) have exceptional elastic modulus, strength, electrical and thermal conductivity, and chemical and thermal stability [69, 70]. In general, aspect ratio of CNTs exceeds 1000, as the length of a carbon nanotube is of the order of micrometers and diameter nanometers. Young's modulus of a SWCNT has been reported to be as high as 5 TPa and for MWCNT $\sim$1.8 TPa [71, 72]. The tensile strength of CNTs can be a hundred times that of steel, while the density is one-sixth to one-seventh of steel [73].

The strength of covalent carbon–carbon bond is the dictating factor for those superior mechanical properties of CNTs. As each carbon atom in the lattice is covalently bonded to three neighboring atoms, this hexagonal structure results in the sp^2 hybridization process. One *s*-orbital and two *p*-orbitals of a carbon atom in its excited state combine to form three hybrid sp^2-orbitals at 120° relative to each other (Fig. 2.14) [74]. The resulting strong covalent bond, σ-bond, is largely responsible for the excellent properties of CNTs. π-bond, which is the out-of-plane bond, is relatively weak. However, this is effectively used during surface chemical modification/grafting and functionalization processes.

As the name indicates, SWCNTs are made of single graphene layer, whereas MWCNTs consist of two or more concentric cylindrical shells of graphene sheets

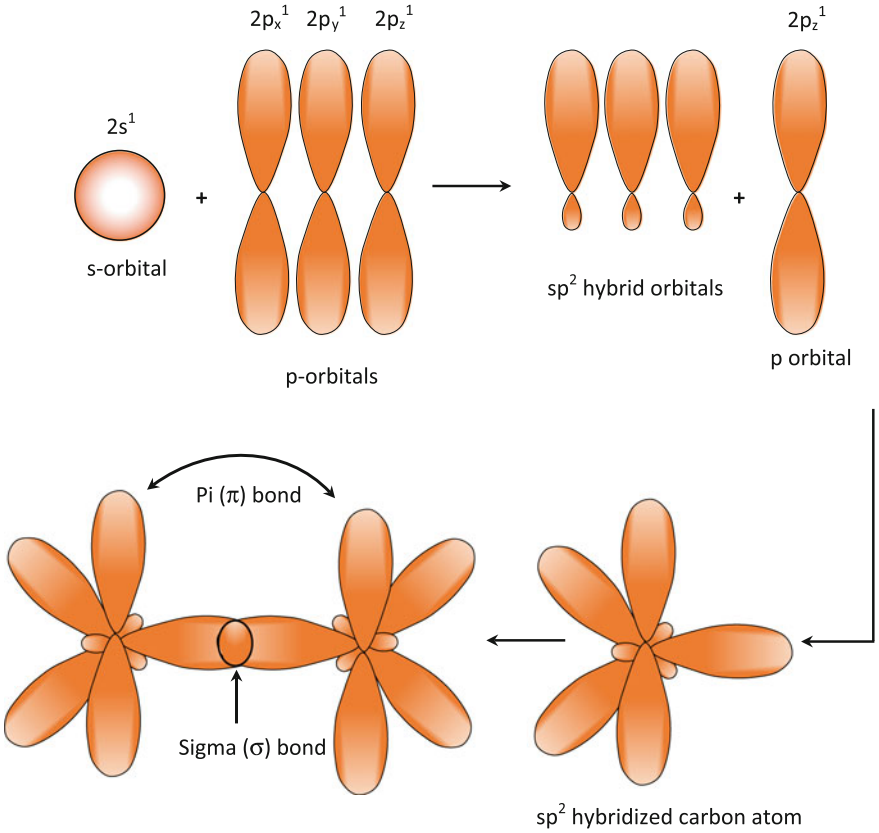

Fig. 2.14 Carbon atoms of CNTs participating in sp^2 hybridization process and resulting in the formation of σ- and π-bonds. Adapted from [74]

coaxially arranged around a central hollow core with interlayer separation as in graphite (0.34 nm). As the planar graphene sheets are folded to make cylinders, the hexagonal symmetry of the carbon atoms is distorted, because the lattice is curved and must match along the edges (with dangling bonds). This leads to a helical arrangement of carbon atoms in the nanotube shells. Depending on the helicity and dimensions of the tubes, the electronic structure changes [75]. It was reported that CNTs can be either metallic or semiconducting. The ends of the cylinders are closed by fullerene-like caps that contain topological defects (pentagons in a hexagonal lattice). Depending on the roll-up, up to three categories of nanotubes can be developed: zigzag, chiral, and armchair (Fig. 2.15) [76]. Clearly, the longer the short side, the larger is the tube diameter. In zigzag tubes, some of the C–C bonds lie parallel to the tube axis, and in the armchair configuration, some C–C bonds are perpendicular to the axis.

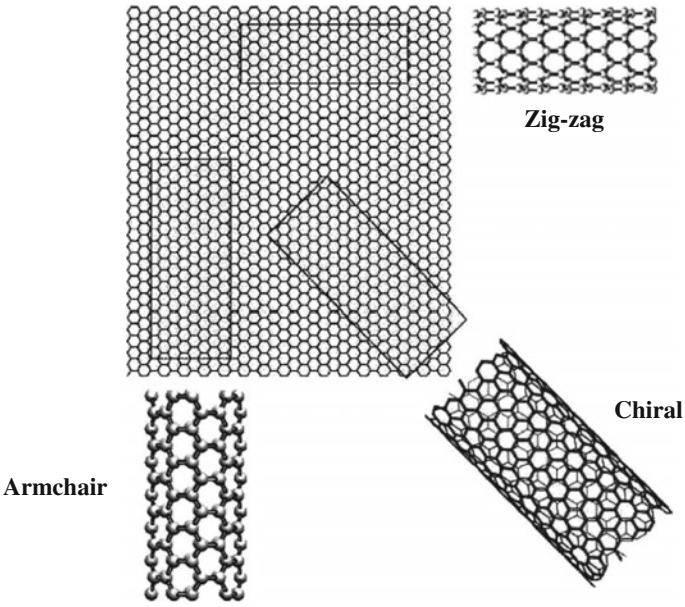

Fig. 2.15 Schematic of different configurations of nanotubes that can be obtained by rolling of a graphene sheet. Reprinted from [76], Copyright (2006), with permission from CRC Press

As the electrons are confined in the radial direction in the singular plane of the graphene sheet, it has been predicted that the tubes with armchair configuration are metallic, whereas zigzag and helical tubes can be either metallic or semiconducting [77]. Conduction in armchair (metallic) tubes occurs through gapless modes because the valence and conduction bands always cross each other at the Fermi energy [78]. In most helical tubes that contain a large number of atoms in the unit cell, the 1D band structure shows an opening of the gap at the Fermi energy, lending it semiconducting properties. This unique electronic behavior occurs only in small nanotubes. As the diameter of the tubes increases, the band gap (which varies inversely with tube diameter) tends toward zero, yielding a zero-gap semiconductor that is equivalent to the planar graphene sheet. In MWCNT, the outer, larger, planar, graphene-like tubes overshadow the electronic structure of the smallest inner tube.

However, the key point is to transfer the potential mechanical, thermal, and electrical properties of the CNTs to the polymer composite. A critical issue to overcome in taking advantage of the superior properties of CNTs is their ability to entangle (and thereby influence dispersion in a polymer matrix). These intertwined networks are a result of high intermolecular van der Waals interactions between the CNTs. Looking at the literature of polymer/CNT nanocomposites, it is reasonable to say that the properties of nanotubes and their potential are not fully transferred to the nanocomposites. Even large variations in the percolation threshold of polymer/CNT materials are noted (see Chap. 3).

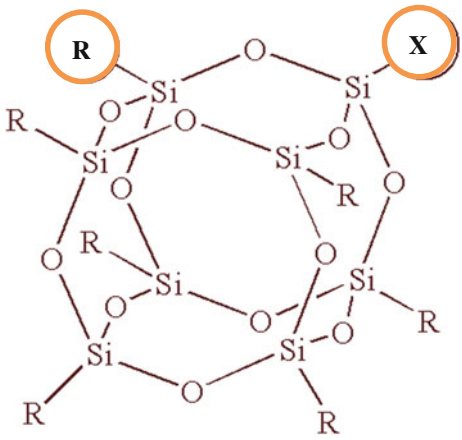

Fig. 2.16 Schematic representation of a POSS particle. *R* is a non-reactive organic group that is generally used for compatibilization and solubilization; and *X* is another functional group that is used for polymerization or grafting

CNTs aside, recently, CNFs are also used to reinforce polymers. CNFs are generally vapor-grown and obtained from pyrolysis of hydrocarbons. For example, Applied Sciences Inc. Pyrograf® Products (ASI), a commercial supplier of different kinds of nanofibers synthesizes CNFs via pyrolytic decomposition of methane in the presence of iron-based catalyst particles at temperatures above 900 °C. Generally, the diameters of CNFs are in the range of 50–200 nm and lengths of 50–100 μm.

2.2.4 *Polyhedral Oligomeric Silsesquioxane*

POSS is molecularly precise, nearly isotropic molecules with hybrid (organic–inorganic) architecture, and their structure contains a stable inorganic Si–O core, which is intermediate ($RSiO_{1.5}$) between silica (SiO_2) and silicones (R_2SiO) [79–84]. The general stoichiometry is $(RSiO_{1.5})_n$, where *n* is 8, 10, or 12 with sizes from 1 to 3 nm in diameter (Fig. 2.16). The core is covered externally by organic substituents that can be modified to present a wide range of polarities and functionalities such as amino, hydroxy, bromo, epoxy, acrylate, cinnamate, fluorine, and maleimide to compatibilize POSS with various polymer systems [79, 85–87]. This great variety results in the diversity of silsesquioxanes. They are synthesized by sol-gel technique, i.e., via hydrolytic condensation of trifunctional monomers $RSiX_3$, X being a highly reactive substituent such as Cl or alkoxy. In general, there are three main kinds of structures in silsesquioxanes: random, ladder-like, and cage-like (including partial cage-like structures) (Fig. 2.17) [85]. More details on the synthesis and types of these condensates that are derived from trifunctional silanes are given in [85].

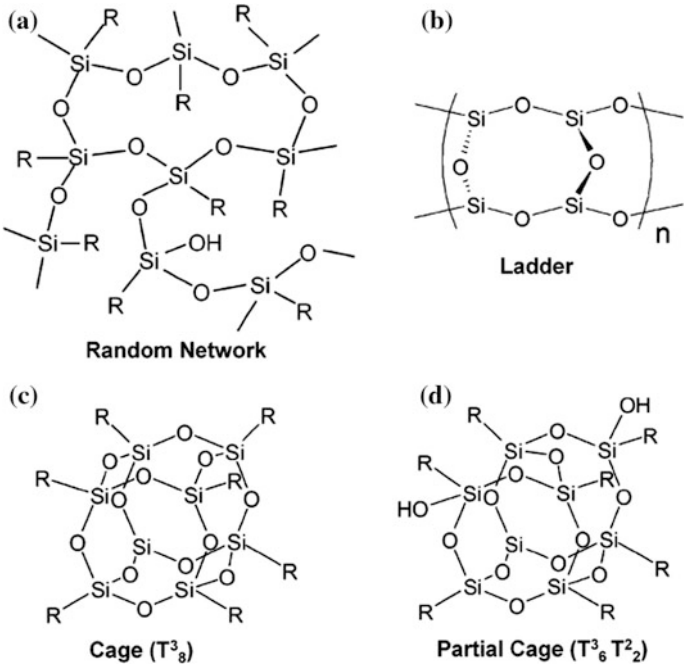

Fig. 2.17 Schematic structures of different types of silsesquioxanes. Octahedral cage structure T^3_8 or in the notation T^a_b: *T* stands for the maximum three siloxane bonds for each silicon, *a* actual number of siloxane bonds on each silicon, and *b* number of silicons in the unit. Reproduced from [85] with permission of The Royal Society of Chemistry, Copyright (2011)

POSS is used to improve the thermal properties of polymers, oxidation resistance, and, in some cases, even mechanical properties. The high thermal stability of POSS (up to ~400 °C) is determined by its chemical structure, such as the bond energy, type of molecules, and reactivity of the bonds. The higher bond energy of Si–O, in particular, yields higher thermal stability. In view of these properties, POSS is also used for a variety of applications as their cage can easily be opened for incorporation of metals (particularly transition metals) and later closed. The range of applications varies from low dielectric constant materials to new resists for electron beam lithography materials and high-temperature lubricants or as active catalysts for organic reactions. More detailed explanations on the synthesis, structure, and properties of these compounds have been given in [72, 88–92].

2.2.5 *Other Equiaxed Nanoparticles*

Over the past few decades, many different methodologies were developed to synthesize equiaxed nanoparticles based on aerosol, sol-gel, plasma or chemical vapor condensation, and wet chemistry techniques. Aerosol methods (comprising flame

hydrolysis, pyrolysis, etc.) usually yield nanoparticles by condensation from a gas phase. Many nanoparticles such as TiO_2, ZrO_2, carbon black, ZnO, Fe_2O_3, SiO_2, CuO, and Al_2O_3 can be obtained through these aerosol methodologies. Even these nanoparticles or masterbatches consisting of resin/nanoparticles are available commercially. For example, Hanse Chemie uses a proprietary *sol-gel*-based synthesis methodology to produce a masterbatch of resin/silica nanoparticles with loadings of up to 40 % silica having sizes in the range of 15–25 nm from aqueous sodium silicate solution.

Laser ablation is also a form of gas condensation process to synthesize nanoparticles. Here, the targets (metal, metal oxide, or semiconductor) are ablated with a pulsated laser [4]; most of the above-mentioned particles can be obtained using this approach along with Mg_2SiO_4, $CaTiO_3$, and $MgAl_2O_4$. A combination of aerosol and sol-gel processes was also adopted to produce SiO_2 nanoparticles; this takes advantage of the low-temperature processing and the ability to produce a large specific area (400 $m^2\ g^{-1}$) due to the low coalescence rate relative to the collision rate; that is, hydrolysis and condensation of TEOS are conducted in a laminar flow chamber at temperatures ranging from ambient to 100 °C [4, 93]. Apart from these techniques, ion implantation was also used as an effective methodology for introducing/embedding particles into the surface layer (up to several micrometers) of a material (polymers, inorganic glasses, ionic crystals, minerals, etc.). This process depends on the implantation parameters such as type of ions, their energy, and current density along with the target properties. A schematic of different stages involved in this process is shown in Fig. 2.18 together with a micrograph of PMMA whose surface has been implanted with Ag nanoparticles [94–96]. Nonetheless, it is important to note that ion implantation process results in radiation-induced defects, polymer structural damage, breakage of covalent bonds, generation of free radicals, cross-linkage, oxidation, etc.

2.2.6 Hierarchical Structured Particles

Recently, there has been a lot of emphasis on the synthesis of hierarchical structured particles for extracting multi-functionality. Examples include immobilization of nanoparticles on porous solids such as clays and zeolites, impregnation of solids/substrates with nanoparticles, and CVD of nanoparticles on micro-/macro-sized particles. Letaïef and Ruiz-Hitzky [97] reported synthesis of a novel class of materials by exfoliating (delaminating) layered silicates containing inorganic network (silica, based on sol-gel process involving hydrolysis of alkoxysilanes) instead of conventional organic network (such as polymer nanocomposites) (Fig. 2.19a). González-Alfaro et al. [98] used sepiolite as a support for immobilizing non-aqueous ferrofluid particles to obtain both superparamagnetic behavior and high adsorption capabilities. Figure 2.19b shows the proposed mechanism of ligands exchange in which the oleic acid-magnetite nanoparticles release some oleic acid molecules, and iron oxide interacts with the silanol surface groups of sepiolite.

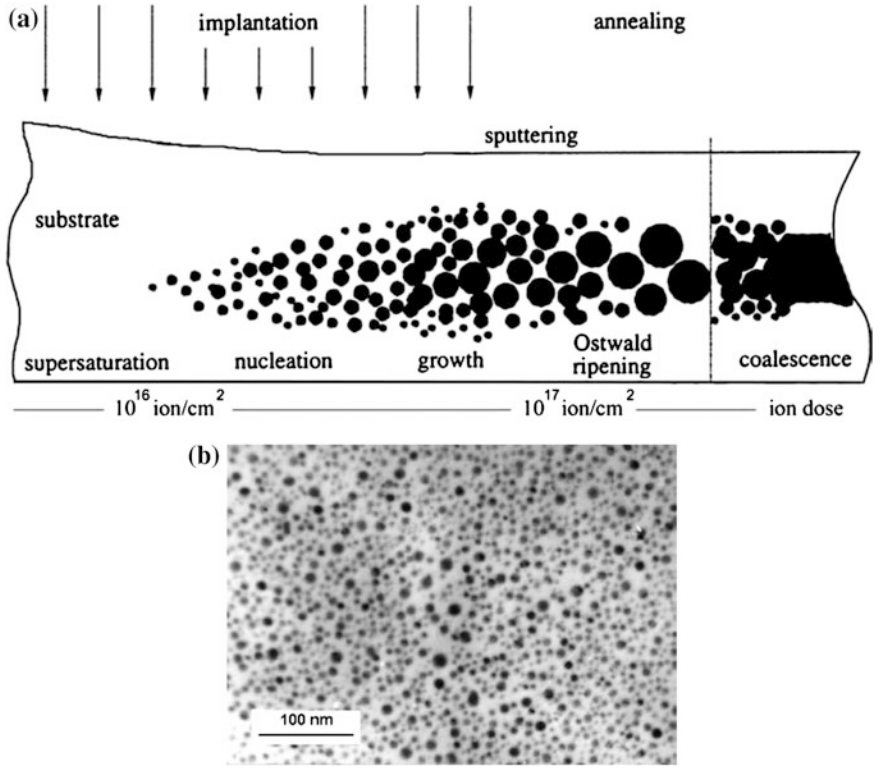

Fig. 2.18 **a** Physical stages involved in nanoparticle synthesis by ion implantation versus ion dose; and **b** a representative sample showing silver nanoparticles produced by Ag^+ implantation into PMMA at 5×10^{16} ion/cm^2. Reproduced from [96] with permission of John Wiley and Sons, Copyright (2005)

In another similar study, Esteban-Cubillo et al. [99] prepared Ag, TiO_2, and Cu functionalized sepiolite by means of a reduction process followed by dehydration of the matrix. As discussed earlier, the structure of sepiolite consists of an arrangement of blocks separated by parallel channels formed by two layers of tetrahedral SiO_2 enclosing a layer of octahedral MgO. Sepiolite, despite its large specific surface area (about 320 m^2/g), has reduced ion exchange capacity so that cations cannot be inserted inside the channels. Instead, acid treatment is used to completely leach out Mg^{2+} cations from the octahedral layer (lixiviation of Mg^{2+}). It is noted that the sepiolite crystalline framework collapses when the fraction of leached Mg^{2+} is greater than or equal to 0.33. Before the collapse, these authors have shown that it is possible to introduce other metallic ions into the octahedral sites using metal alkoxides as starting reagents in which the organic moieties facilitate their diffusion. The advantage of this process is that the nanoparticles are embedded in the silicate particles, rather than being loosely held. An example of this is shown in Fig. 2.20.

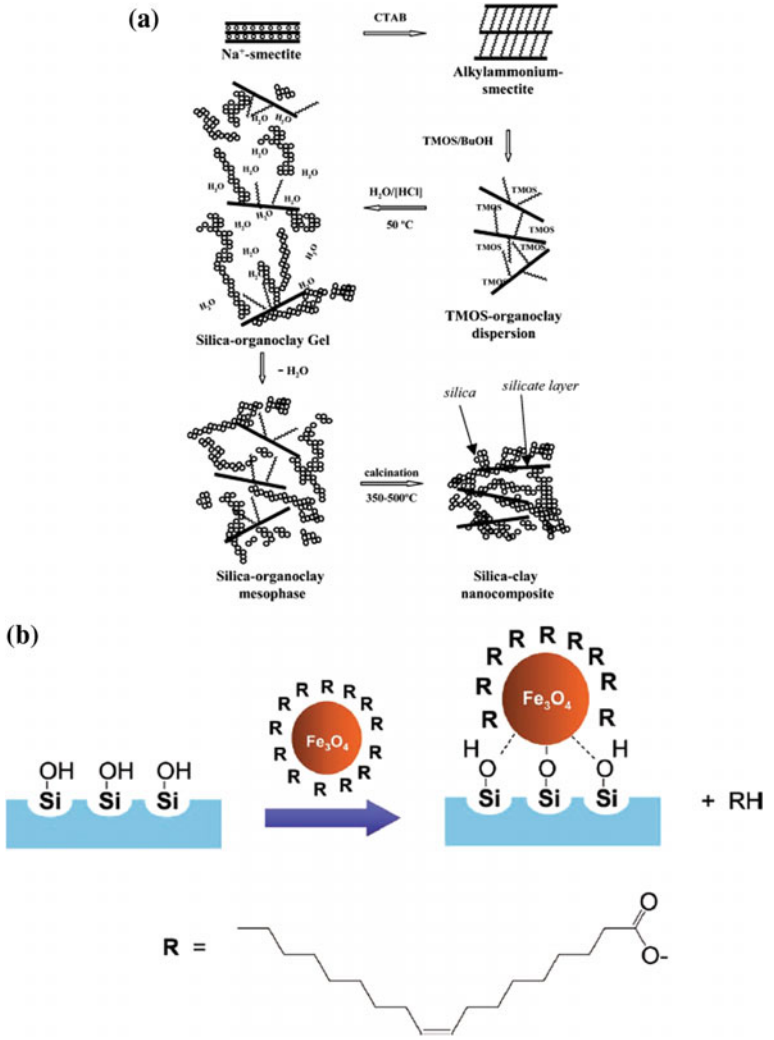

Fig. 2.19 **a** Schematic showing the synthesis procedure of the silica–clay nanocomposites; and **b** proposed mechanism for immobilizing nanoparticles through interactions with surface hydroxyl groups. (**a**) is reproduced from [97] with permission of The Royal Society of Chemistry, Copyright (2003); and (**b**) is reproduced from [98] with permission of John Wiley and Sons, Copyright (2011)

In another methodology to impart superior mechanical and functional properties to traditional fiber-reinforced composites, CNTs are introduced onto carbon fibers [100] and plain woven carbon fiber fabrics [101]. Du et al. [100] used a flame (ethanol) process in the presence of Ni catalyst to introduce CNTs instead of using a conventional CVD process (Fig. 2.21). A nanomanipulator attached to an atomic force microscope inside the SEM chamber has also been used to calculate the bonding force between a CNT and carbon fiber. It is seen that the peeling force

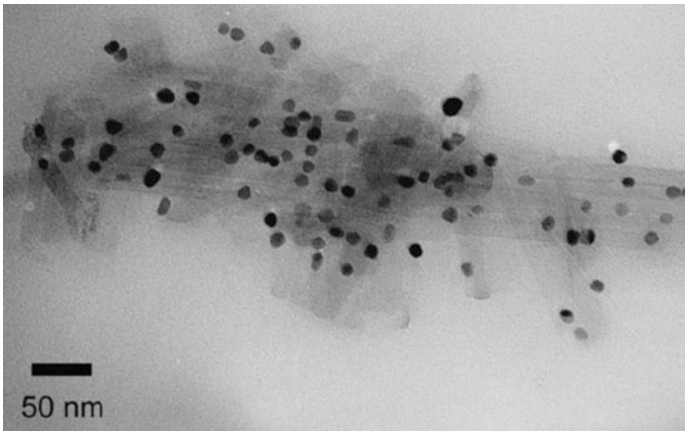

Fig. 2.20 TEM micrograph showing Ni–sepiolite complex. Reprinted from [99], Copyright (2008), with permission from Elsevier

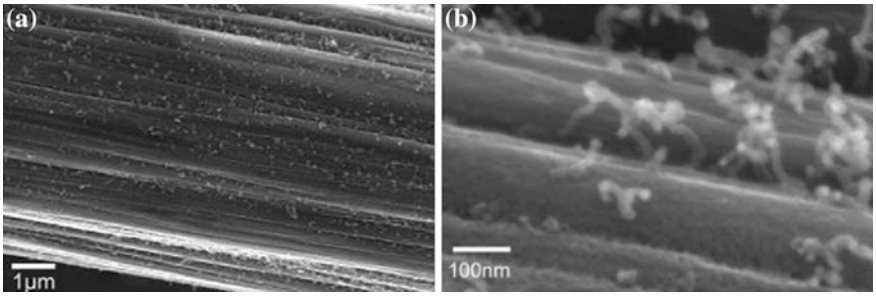

Fig. 2.21 SEM images of CNTs–carbon fiber complex at different magnifications. CNTs are introduced using a flame process with 0.01 M Ni^{2+} catalyst. Reprinted from [100], Copyright (2012), with permission from Elsevier

increases gradually to a maximum of 307 nN as the CNT length is stretched by ~25 nm before detaching from the substrate. In [101], the plain woven fabrics with CNTs are used to prepare epoxy-based composites (16 plies via hand lay-up method). Mode I and Mode II interlaminar fracture toughness values of these composite laminates show drastic improvements of 67 and 60 %, respectively. It is also interesting to note that the failure mechanisms of composites with and without CNTs are different. In mode I condition, fabrics without CNTs are dominated by carbon fiber–epoxy interfacial failure, but cohesive CNTs/epoxy matrix failure between CNTs/carbon fiber and on carbon fiber surfaces is dominant with fabrics containing CNTs. Beyond these, several other hybrid materials based on CNTs and metal nanoparticles are reported in view of applications that demand catalytic and magnetic properties, e.g., Fe_3O_4 nanoparticles decorated MWCNTs [102] and gold nanoparticles functionalized SWCNTs [103].

Irrespective of the different functionalities of these engineered nanoparticles, it is important to maintain their functionality even after their incorporation into polymers. To achieve this, first and foremost issue to deal with is the dispersion and distribution of these particles in a polymer matrix, which of course is closely associated with the compatibility between particles and matrix. These are the topics that will be discussed in more details in Chap. 3.

References

1. Auffan M, Rose J, Bottero JY, Lowry GV, Jolivet JP, Wiesner MR (2009) Towards a definition of inorganic nanoparticles from an environmental, health and safety perspective. Nat Nanotechnol 4:634–641
2. Yokoyama T (2008) Basic properties and measuring methods of nanoparticles. In: Hosokawa M, Nogi K, Naito M, Yokoyama T (eds) Nanoparticle technology handbook. Elsevier, Amsterdam, pp 3–48
3. Nagarajan R (2008) Nanoparticles: building blocks for nanotechnology. In: Nagarajan R, Hatton TA (eds) Nanoparticles: synthesis, stabilization, passivation, and functionalization, ACS Symposium Series, American Chemical Society, vol. 996, pp 2–14
4. Ash BJ, Eitan A, Schadler LS (2004) Polymer nanocomposites with particle and carbon nanotube fillers. In: Schwarz JA, Contescu CI, Putyera K (eds) Dekker encyclopedia of nanoscience and nanotechnology. CRC Press, Boca Raton, pp 2917–2930
5. Yean S, Cong I, Yavuz CT, Mayo JT, Yu WW, Kan AT, Colvin VL, Tomson MB (2005) Effect of magnetite particle size on adsorption and desorption of arsenite and arsenate. J Mater Res 20:3255–3264
6. Stumm W, Morgan JJ (1981) Aquatic chemistry: an introduction emphasizing chemical equilibria in natural waters, 2nd edn. Wiley-Interscience, New York, p 780
7. Auffan M, Rose J, Proux O, Borschneck D, Masion A, Chaurand P, Hazemann JL, Chaneac C, Jolivet JP, Wiesner MR, Geen AV, Bottero JY (2008) Enhanced adsorption of arsenic onto nano-maghemites: As(III) as a probe of the surface structure and heterogeneity. Langmuir 24:3215–3222
8. Lamber R, Wetjen S, Jaeger NI (1995) Size dependence of the lattice parameter of small palladium particles. Phys Rev B 51:10968–10971
9. Jolivet JP, Froidefond C, Pottier A, Chanéac C, Cassaignon S, Tronc E, Euzen P (2004) Size tailoring of oxide nanoparticles by precipitation in aqueous medium. A semi-quantitative modelling. J Mater Chem 14:3281–3288
10. Uchino K, Sadanaga E, Hirose T (1989) Dependence of the crystal structure on particle size in barium titanate. J Am Ceram Soc 72:1555–1558
11. Jolivet JP, Barron AR (2007) Nanomaterials fabrication. In: Wiesner MR, Bottero JY (eds) Environmental nanotechnology: applications and impacts of nanomaterials. McGraw Hill, New York, pp 29–103
12. Morones JR, Elechiguerra JL, Camacho A, Holt K, Kouri JB, Ramírez JT, Yacaman MJ (2005) The bactericidal effect of silver nanoparticles. Nanotechnology 16:2346–2353
13. Sun XC (2002) Microstructure characterization and magnetic properties of nanomaterials. Mol Phys 100:3059–3063
14. Chernyshev AP (2009) Effect of nanoparticle size on the onset temperature of surface melting. Mater Lett 63:1525–1527
15. Nanda KK (2007) Size-dependent melting of nanoparticles: hundred years of thermodynamic model. Pramana—J Phys 72:617–628

16. Zhang M, Efremov MY, Schiettekatte F, Olson EA, Kwan AT, Lai SL, Wisleder T, Greene JE, Allen LH (2000) Size-dependent melting point depression of nanostructures: nanocalorimetric measurements. Phys Rev B 62:10548–10557
17. Lai SL, Guo JY, Petrova V, Ramanath G, Allen LH (1996) Size-dependent melting properties of small tin particles: nanocalorimetric measurements. Phys Rev Lett 77:99–102
18. Smitha SL, Gopchandran KG, Smijesh N, Philip R (2013) Size-dependent optical properties of Au nanorods. Prog Nat Sci Mater Int 23:36–43
19. Pavlidou S, Papaspyrides CD (2008) A review on polymer-layered silicate nanocomposites. Prog Polym Sci 33:1119–1198
20. Murray HH (2007) Structure and composition of the clay minerals and their physical and chemical properties. In: Applied clay mineralogy: occurrences, processing and applications of kaolins, bentonites, palygorskitesepiolite, and common clays. Elsevier, Amsterdam, pp 7–32
21. LeBaron PC, Wang Z, Pinnavaia TJ (1999) Polymer-layered silicate nanocomposites: an overview. Appl Clay Sci 15:11–29
22. Brigatti MF, Galan E, Theng BKG (2006) Structures and mineralogy of clay minerals. In: Bergaya F, Theng BKG, Lagaly G (eds) Developments in clay science, vol 1. Elsevier, Amsterdam, pp 19–86
23. Carrado KA, Decarreau A, Petit S, Bergaya F, Lagaly G (2006) Synthetic clay minerals and purification of natural clays. In: Bergaya F, Theng BKG, Lagaly G (eds) Developments in clay science, vol 1. Elsevier, Amsterdam, pp 115–139
24. Okamoto M (2007) Recent advances in polymer/layered silicate nanocomposites: an overview from science to technology. In: Advani SG (ed) Processing and properties of nanocomposites. World Scientific Publishing Co. Pte. Ltd., Singapore, pp 247–305
25. Hillier S (2003) Chlorite in sediments, sedimentology, encyclopedia of earth science. Springer, Netherlands, pp 195–202
26. Bilotti E, Fischer HR, Peijs T (2008) Polymer nanocomposites based on needle-like sepiolite clays: effect of functionalized polymers on the dispersion of nanofiller, crystallinity, and mechanical properties. J Appl Polym Sci 107:1116–1123
27. Dasari A, Yu ZZ, Mai Y-W, Unpublished work
28. PetroTech Associates, http://www.petrotech-assoc.com/prod01.htm. Accessed 10 Oct 2015
29. Giannelis EP, Krishnamoorti R, Manias E (1999) Polymer-silicate nanocomposites: model systems for confined polymers and polymer brushes. In: Polymers in confined environments, advances in polymer science, vol 138, pp 107–147
30. Ray SS, Okamoto M (2003) Polymer/layered silicate nanocomposites: a review from preparation to processing. Prog Polym Sci 28:1539–1641
31. Tjong SC (2006) Structural and mechanical properties of polymer nanocomposites. Mater Sci Eng Rep 53:73–197
32. Utracki LA (2004) Clay-containing polymeric nanocomposites, vol 1. iSmithers Rapra Publishing, Shawbury, p 785
33. Tjong SC (2006) Synthesis and structure-property characteristics of clay-polymer nanocomposites. In: Nanocrystalline materials. Elsevier, Oxford, pp 311–348
34. Fornes TD, Hunter DL, Paul DR (2004) Effect of sodium montmorillonite source on nylon 6/clay nanocomposites. Polymer 45:2321–2331
35. Fornes TD, Hunter DL, Paul DR (2004) Nylon-6 nanocomposites from alkylammonium-modified clay: the role of alkyl tails on exfoliation. Macromolecules 37:1793–1798
36. Fornes TD, Yoon PJ, Hunter DL, Keskkula H, Paul DR (2002) Effect of organoclay structure on nylon 6 nanocomposite morphology and properties. Polymer 43:5915–5933
37. Fornes TD, Yoon PJ, Keskkula H, Paul DR (2001) Nylon 6 nanocomposites: the effect of matrix molecular weight. Polymer 42:9929–9940
38. Taviot-Gueho C, Leroux F (2006) In situ polymerization and intercalation of polymers in layered double hydroxides. In: Duan X, Evans DG (eds) Layered double hydroxides, vol 119. Springer, Berlin, pp 121–159

39. Moujahid EM, Besse JP, Leroux F (2002) Synthesis and characterization of a polystyrene sulfonate layered double hydroxide nanocomposite. In-situ polymerization vs. polymer incorporation. J Mater Chem 12:3324–3333
40. Oriakhi CO, Farr IV, Lerner MM (1996) Incorporation of poly(acrylic acid), poly (vinylsulfonate) and poly(styrenesulfonate) within layered double hydroxides. J Mater Chem 6:103–107
41. Li L, Ma RZ, Ebina Y, Iyi N, Sasaki T (2005) Positively charged nanosheets derived via total delamination of layered double hydroxides. Chem Mater 17:4386–4391
42. Wang Z, Pinnavaia TJ (1998) Hybrid organic-inorganic nanocomposites: exfoliation of magadiite nanolayers in an elastomeric epoxy polymer. Chem Mater 10:1820–1826
43. Schadler LS (2004) Polymer-based and polymer-filled nanocomposites. In: Ajayan PM, Schadler LS, Braun PV (eds) Nanocomposite science and technology. Wiley-VCH Verlag GmbH & Co. KGaA, Weinheim, pp 77–153
44. Stankovich S, Dikin DA, Dommett GHB, Kohlhaas KM, Zimney EJ, Stach EA, Piner RD, Nguyen ST, Ruoff RS (2006) Graphene-based composite materials. Nature 442:282–286
45. Chung DDL (2002) Review graphite. J Mater Sci 37:1475–1489
46. Chung DDL (1987) Exfoliation of graphite. J Mater Sci 22:4190–4198
47. Katsnelson MI (2007) Graphene: carbon in two dimensions. Mater Today 10:20–27
48. Li D, Kaner RR (2008) Graphene-based materials. Science 320:1170–1171
49. Geim AK, Novoselov KS (2007) The rise of graphene. Nat Mater 6:183–191
50. Meyer JC, Geim AK, Katsnelson MI, Novoselov KS, Booth TJ, Roth S (2007) The structure of suspended graphene sheets. Nature 446:60–63
51. Berger C, Song ZM, Li XB, Wu XS, Brown N, Naud C, Mayou D, Li T, Hass J, Marchenkov AN, Conrad EH, First PN, de Heer WA (2006) Electronic confinement and coherence in patterned epitaxial graphene. Science 312:1191–1196
52. Wu JS, Pisula W, Mullen K (2007) Graphenes as potential material for electronics. Chem Rev 107:718–747
53. Eda G, Fanchini G, Chhowalla M (2008) Large-area ultrathin films of reduced graphene oxide as a transparent and flexible electronic material. Nat Nanotechnol 3:270–274
54. Brodie BC (1859) On the atomic weight of graphite. Philos Trans R Soc Lond 149:249–259
55. Staudenmaier L (1898) Verfahren zur Darstellung der Graphitsäure. Ber Dtsch Chem Ges 31:1481–1487
56. Hummers WS, Offeman RE (1958) Preparation of graphitic oxide. J Am Chem Soc 80:1339
57. Dresselhaus MS, Dresselhaus G (2002) Intercalation compounds of graphite. Adv Phys 51:1–186
58. Lerf A, He H, Forster M, Klinowski J (1998) Structure of graphite oxide revisited. J Phys Chem B 102:4477–4482
59. Dreyer DR, Park S, Bielawski CW, Ruoff RS (2010) The chemistry of graphene oxide. Chem Soc Rev 39:228–240
60. Compton OC, Nguyen ST (2010) Graphene oxide, highly reduced graphene oxide, and graphene: versatile building blocks for carbon-based materials. Small 6:711–723
61. Stankovich S, Dikin DA, Dommett GHB, Kohlhaas KM, Zimney EJ, Stach EA, Piner RD, Nguyen ST, Ruoff RS (2006) Graphene-based composite materials. Nature 442:282–286
62. Stankovich S, Piner RD, Nguyen ST, Ruoff RS (2006) Synthesis and exfoliation of isocyanate-treated graphene oxide nanoplatelets. Carbon 44:3342–3347
63. Boehm HP, Clauss A, Fischer GO, Hofmann U (1962) Das Adsorptionsverhalten sehr dünner Kohlenstoff-Folien. Zeitschrift für anorganische und allgemeine Chemie 316:119–127
64. McAllister MJ, Li JL, Adamson DH, Schniepp HC, Abdala AA, Liu J, Herrera-Alonso M, Milius DL, Car R, Prud'homme RK, Aksay IA (2007) Single sheet functionalized graphene by oxidation and thermal expansion of graphite. Chem Mater 19:4396–4404

65. Kudin KN, Ozbas B, Schniepp HC, Prud'homme PK, Aksay IA, Car R (2008) Raman spectra of graphite oxide and functionalized graphene sheets. Nano Lett 8:36–41
66. Dubin S, Gilje S, Wang K, Tung VC, Cha K, Hall AS (2010) A one-step solvothermal reduction method for producing reduced graphene oxide dispersions in organic solvents. ACS Nano 4:3845–3852
67. Shen YX, Zhang HB, Zhang H, Ren W, Dasari A, Tang GS, Yu ZZ (2013) Structural evolution of functionalized graphene sheets during solvothermal reduction. Carbon 56:132–138
68. Iijima S (1991) Helical microtubules of graphitic carbon. Nature 354:56–58
69. Ebbesen TW, Ajayan PM (1992) Large-scale synthesis of carbon nanotubes. Nature 358:220–222
70. Ruoff RS, Lorents DC (1995) Mechanical and thermal properties of carbon nanotubes. Carbon 33:925–930
71. Treacy MMJ, Ebbesen TW, Gibson JM (1996) Exceptionally high Young's modulus observed for individual carbon nanotubes. Nature 381:678–680
72. Wong EW, Sheehan PE, Lieber CM (1997) Nanobeam mechanics: elasticity, strength, and toughness of nanorods and nanotubes. Science 277:1971–1975
73. Chen WX, Li F, Han G, Xia JB, Wang LY, Tu JP, Xu ZD (2003) Tribological behavior of carbon-nanotube-filled PTFE composites. Tribol Lett 15:275–278
74. Wernik JA, Meguid SA (2010) Recent developments in multifunctional nanocomposites using carbon nanotubes. Appl Mech Rev 63:050801–050840
75. Mintmire JW, Dunlap BI, White CT (1992) Are fullerene tubules metallic? Phys Rev Lett 68:631–634
76. Fischer J (2006) Carbon nanotubes: structure and properties. In: Gogotsi Y (ed) Nanotubes and Nanofibers. CRC Press, Boca Raton, pp 1–36
77. Ajayan PM, Ebbesen TW (1997) Nanometre-size tubes of carbon. Rep Prog Phys 60:1025
78. Wilder JWG, Venema LC, Rinzler AG, Smalley RE, Dekker C (1998) Electronic structure of atomically resolved carbon nanotubes. Nature 391:59–62
79. Zhang Y, Lee S, Yoonessi M, Liang K, Pittman CU (2006) Phenolic resin–trisilanolphenyl polyhedral oligomeric silsesquioxane (POSS) hybrid nanocomposites: structure and properties. Polymer 47:2984–2996
80. Zhao Y, Schiraldi D (2005) Thermal and mechanical properties of polyhedral oligomeric silsesquioxane (POSS)/polycarbonate composites. Polymer 46:11640–11647
81. Jash P, Wilkie C (2005) Effects of surfactants on the thermal and fire properties of poly (methyl methacrylate)/clay nanocomposites. Polym Degrad Stab 88:401–406
82. Fina A, Abbenhuis H, Tabuani D, Camino G (2006) Metal functionalized POSS as fire retardants in polypropylene. Polym Degrad Stab 91:2275–2281
83. Fina A, Tabuani D, Carniato F, Frache A, Boccaleri E, Camino G (2006) Polyhedral oligomeric silsesquioxanes (POSS) thermal degradation. Thermochim Acta 440:36–42
84. Devaux E, Rochery M, Bourbigot S (2002) Polyurethane/clay and polyurethane/POSS nanocomposites as flame retarded coating for polyester and cotton fabrics. Fire Mater 26:149–154
85. Kanamoria K, Nakanishi K (2011) Controlled pore formation in organotrialkoxysilane-derived hybrids: from aerogels to hierarchically porous monoliths. Chem Soc Rev 40:754–770
86. Liu L, Hu Y, Song L, Nazare S, He S, Hull R (2007) Combustion and thermal properties of OctaTMA-POSS/PS composites. J Mater Sci 42:4325–4333
87. Liu YL, Chang GP (2006) Novel approach to preparing epoxy/polyhedral oligometric silsesquioxane hybrid materials possessing high mass fractions of polyhedral oligometric silsesquioxane and good homogeneity. J Polym Sci Part A: Polym Chem 44:1869–1876
88. Schiraldi DA, Iyer S (2010) What does it take to make a stable POSS/polymer composite? In: Advances in silicones and silicone-modified materials, ACS Symposium Series, American Chemical Society, vol 1051, pp 211–226

89. Lickiss PD, Rataboul F (2009) Fully condensed polyhedral oligosilsesquioxanes (POSS): from synthesis to application. ChemInform 40:1–116
90. Carniato F, Boccaleri E, Marchese L, Fina A, Tabuani D, Camino G (2007) Synthesis and characterisation of metal isobutylsilsesquioxanes and their role as inorganic-organic nanoadditives for enhancing polymer thermal stability. Eur J Inorg Chem 2007:585–591
91. Edelmann FT (1992) Model compounds for metal oxides on SiO_2 surfaces. Angew Chem Int Ed Engl 31:586–587
92. Lichtenhan JD, Vu NQ, Carter JA, Gilman JW, Feher FJ (1993) Silsesquioxane-siloxane copolymers from polyhedral silsesquioxanes. Macromolecules 26:2141–2142
93. Hyeon-Lee J, Beaucage G, Pratsinis SE (1997) Aero-sol-gel synthesis of nanostructured silica powders. Chem Mater 9:2400–2403
94. Stepanov A (2004) Optical properties of metal nanoparticles synthesized in a polymer by ion implantation: a review. Tech Phys 49:143–153
95. Townsend PD (1987) Optical effects of ion implantation. Rep Prog Phys 50:501–558
96. Stepanov AL (2005) Optical extinction of metal nanoparticles synthesized in polymer by ion implantation. In: Nicolais L, Carotenuto G (eds) Metal-polymer nanocomposites. Wiley, Hoboken, pp 241–263
97. Letaief S, Ruiz-Hitzky E (2003) Silica-clay nanocomposites. Chem Commun 24:2996–2997
98. González-Alfaro Y, Aranda P, Fernandes FM, Wicklein B, Darder M, Ruiz-Hitzky E (2011) Multifunctional porous materials through ferrofluids. Adv Mater 23:5224–5228
99. Esteban-Cubillo A, Pina-Zapardiel R, Moya JS, Barba MF, Pecharroman C (2008) The role of magnesium on the stability of crystalline sepiolite structure. J Eur Ceram Soc 28:1763–1768
100. Du X, Liu HY, Zhou C, Moody S, Mai Y-W (2012) On the flame synthesis of carbon nanotubes grafted onto carbon fibers and the bonding force between them. Carbon 50:2347–2374
101. Du X, Liu HY, Xu F, Zeng Y, Mai Y-W (2014) Flame synthesis of carbon nanotubes onto carbon fiber woven fabric and improvement of interlaminar toughness of composite laminates. Compos Sci Technol 101:159–166
102. Fan XJ, Li X (2012) Preparation and magnetic property of multiwalled carbon nanotubes decorated by Fe_3O_4 nanoparticles. New Carbon Mater 27:111–116
103. Salice P, Gambarin A, Daldosso N, Mancin F, Menna E (2014) Noncovalent interaction between single-walled carbon nanotubes and pyrene-functionalized gold nanoparticles in water-soluble nanohybrids. J Phys Chem C 118:27028–27038

http://www.springer.com/978-1-4471-6807-2

Polymer Nanocomposites
Towards Multi-Functionality
Dasari, A.; Yu, Z.-Z.; Mai, Y.-W.
2016, XII, 305 p. 196 illus., 72 illus. in color., Hardcover
ISBN: 978-1-4471-6807-2